Solar Energy Materials & Solar Cells 95 (2011) 2264–2271

Contents lists available at ScienceDirect

Solar Energy Materials & Solar Cells

journal homepage: www.elsevier.com/locate/solmat

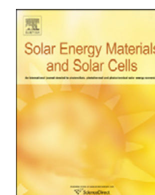

# Correlating internal stresses, electrical activity and defect structure on the micrometer scale in EFG silicon ribbons

G. Sarau [a,b,c,*], S. Christiansen [a,c], M. Holla [d,e], W. Seifert [d,e]

[a] Institute of Photonic Technology, Albert-Einstein-Street 9, D-07745 Jena, Germany
[b] Max Planck Institute of Microstructure Physics, Weinberg 2, D-06120 Halle, Germany
[c] Max Planck Institute for the Science of Light, Günther-Scharowsky-Street 1, D-91058 Erlangen, Germany
[d] IHP, Im Technologiepark 25, D-15236 Frankfurt (Oder), Germany
[e] Joint Laboratory IHP/BTU, Brandenburg University of Technology, Konrad-Wachsmann-Allee 1, D-03046 Cottbus, Germany

ARTICLE INFO

*Article history:*
Received 19 October 2010
Received in revised form
16 March 2011
Accepted 22 March 2011
Available online 13 April 2011

*Keywords:*
Internal stresses
Recombination activity
Microstructure
Multicrystalline silicon
Dislocations
Raman

ABSTRACT

In the present paper, we study the influence of defects through their stress fields on the electrical activity and residual stress states of as-grown edge-defined film-feed (EFG) multicrystalline silicon (mc-Si) ribbons. We apply a combination of micro-Raman spectroscopy, electron beam induced current, defect etching and electron backscatter diffraction techniques that enables us to correlate internal stresses, recombination activity and microstructure on the micrometer scale. The stress fields of defect structures are considered to be too small (several tens of MPa) to influence directly the electrical activity, but they can enhance it via stress-induced accumulation of metallic impurities. It is commonly found that not all recombination-active dislocations on grain boundaries (GBs) and within grains are accompanied by internal stresses. The reason for this is that dislocations interact with each other and tend to locally rearrange in configurations of minimum strain energy in which their stress fields can cancel partially, totally or not at all. The outcome is a nonuniform distribution of electrical activity and internal stresses along the same GB, along different GBs of similar character as well as inside the same grain and inside different grains of similar crystallographic orientations. Our work has implications for developing crystal growth procedures that may lead to reduced internal stresses and consequently to improved electrical quality and mechanical stability of mc-Si materials by means of controlled interaction between structural defects.

© 2011 Elsevier B.V. All rights reserved.

## 1. Introduction

EFG silicon ribbon growth technology has been developed as a cost-effective alternative to ingot- and block-cast crystal growth technologies due to its low silicon consumption. The silicon ribbons are grown directly from the melt at the desired thickness and cut in wafers by a laser without saw-induced kerf losses [1]. Future directions towards even a more cost-efficient EFG technology include a reduction in the tube thickness $t$, an increase in the tube face width $w$ and in the growth speed [1–3].

These developments are hindered by the thermally induced stresses characteristic for the EFG silicon growth. They are produced by (1) the steep vertical temperature gradients of $\sim$1000 °C cm$^{-1}$ at the melt–crystal interface needed to accommodate the latent heat of crystallization, (2) the curvature of the crystallization front, (3) the mechanical constrains due to continuity of displacements imposed at the tube edges, and (4) the rapid cooling [1,2,4]. Since the temperature gradients vary as $t^{-2}$, they increase with decrease in tube thickness leading to an increase in the thermal stresses acting on the tube [2]. Above the brittle–ductile transition temperature of silicon, these stresses can relax partly or totally during ribbon growth by plastic deformation including in-plane creep, out-of-plane buckling and the formation of extended lattice defects such as dislocations, low-angle grain boundaries, cracks and their combinations. Below this temperature, the remaining thermal stresses are incorporated as thermally induced residual stresses in the EFG tube [2,3,5]. In particular, the critical stress for buckling, which is proportional to $(t/w)^2$ limits both the decrease in the tube thickness and the increase in the tube width [2,5]. Thermal stresses are also limiting the growth speed [2]. Another important constraint in the EFG growth of stable thinner silicon tubes is the thickness variation of

* Corresponding author at: Max Planck Institute for the Science of Light, Günther-Scharowsky-Street 1, D-91058 Erlangen, Germany. Tel.: +49 9131 6877552; fax: +49 9131 6877499.
*E-mail addresses:* george.sarau@mpl.mpg.de (G. Sarau), silke.christiansen@mpl.mpg.de (S. Christiansen), markus.holla@tu-cottbus.de (M. Holla), seifert@ihp-microelectronics.com (W. Seifert).

0927-0248/$ - see front matter © 2011 Elsevier B.V. All rights reserved.
doi:10.1016/j.solmat.2011.03.039

up to ± 30 μm across the face width as a result of small horizontal temperature differences of the order of 1–2 °C along the meniscus region [2,6].

Moreover, the grown-in thermally induced residual stresses combined with an unfavorable arrangement of crystal defects having their own stress fields, their superposition is referred to as internal stresses, may couple critically with external mechanical and thermal loads. This may happen during production and handling of wafers/cells and modules leading to unpredictable breakage and additional defects [7–9]. Therefore, understanding and controlling the internal and external stresses are crucial to ensure the mechanical integrity of the EFG wafers/cells as well as to reduce the density of stress-induced defects, which are commonly recombination active, thus improving both process yields and solar cell efficiencies.

Internal shear stresses in EFG and string silicon ribbons have been found mainly at twin and grain boundaries by infrared photoelasticity method known also as infrared birefringence imaging with a spatial resolution of 5 μm/pixel and a sensitivity of ± 1.5 MPa in the best case [8,10–13]. The micro-Raman technique used in the present study is able to probe very concentrated stress distributions originating from structural defects by scanning point-by-point spectra that can be averaged over larger areas if needed [14,15]. Its depth and lateral resolutions depend on the laser excitation wavelength ranging from μm to nm, while its sensitivity is better than ± 12.5 MPa [16,17]. By comparison, photoelasticity is not able to resolve such stress concentrations but it is much better in probing small thermally induced residual stresses since it integrates the signal over the entire thickness of the sample.

It has been observed that high stressed areas show high electron–hole lifetimes [8,12]. So far such correlated investigations have been performed at large scales. However, our previous studies as well as other studies demonstrate the importance of the local variations in properties for a deeper understanding of the solar silicon materials for higher mechanical stability and solar energy conversion efficiencies [16,18–21].

In this work, we correlate mechanical, electrical, and structural properties of as-grown EFG silicon ribbon material on the micrometer scale. For this purpose, we combine at identical positions micro-Raman spectroscopy for measuring μm-scaled internal stress fields, electron beam induced current (EBIC) for evaluating the recombination activity, defect etching for the optical visualization of surface defects, and electron backscatter diffraction (EBSD) for determining the grain orientations and grain boundary types. Our results are discussed in relation to the EFG crystallization process and the existing studies.

## 2. Experimental details

Commercially available p-type EFG mc-Si material showing about 15.2% cell efficiency after in-line processing has been investigated in this work. Four pieces were cut from different as-grown wafers (125 × 125 mm, mean wall thickness of 200 μm) originating from various heights or faces of an octagonal EFG tube (see Fig. 1(a)) grown under optimal conditions with a speed of 1 cm/min [3]. Prior to the Raman measurements, the samples surface was evened out by mechanical polishing to ensure stress measurements that are not affected by uncontrolled reflections at rough surface facets. We applied a standard polishing procedure changing gradually from larger to smaller diamond particle sizes with the final polishing step removing most of the previously damaged surface layer and thus leaving the samples in a negligible polishing-induced stress state. After polishing, the samples were Secco-etched [22] for 5 s to make the grain boundaries and dislocations visible. The results presented in this paper are representative for the investigated samples being obtained on a piece of 18 × 20 mm shown in Fig. 1(b), which was cut from the center of an as-grown EFG wafer.

The Raman stress measurements were performed at room temperature in the backscattering configuration using a LabRam HR800 spectrometer from Horiba Jobin Yvon. A He–Ne laser with an excitation wavelength of 633 nm was employed resulting in a

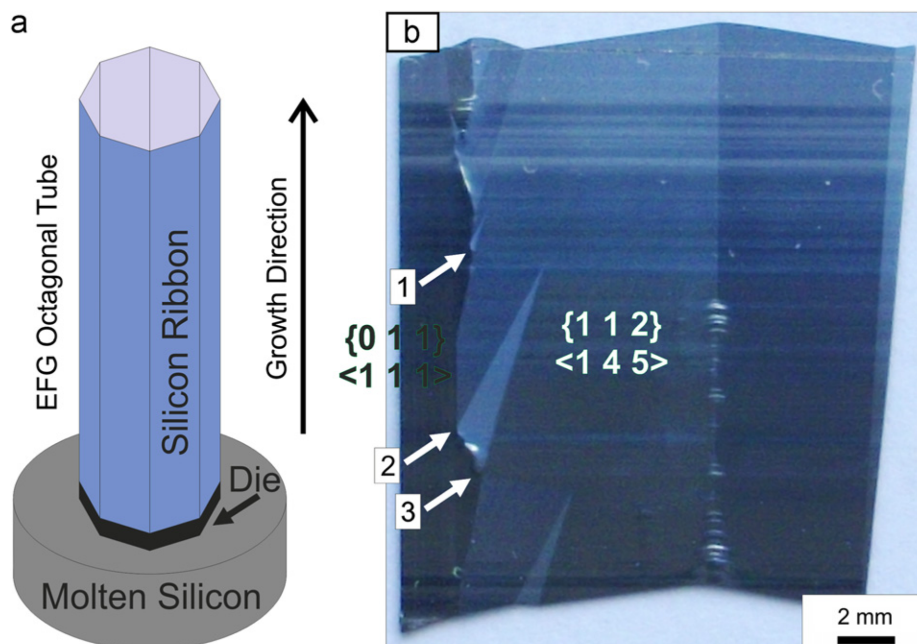


**Fig. 1.** (a) Schematic of the EFG crystal growth process (not to scale). (b) Optical image of a piece cut from the center of an as-grown EFG wafer. Three representative positions indicated by arrows have been chosen to illustrate the correlation between internal stresses, electrical activity and microstructure. They are situated along a GB that typically occurs between two adjacent grains of {0 1 1} and {1 1 2} orientations characteristic for steady-state EFG growth. The buckling deformation is visible.

penetration depth of a few μm in silicon. For the 100 × objective (numerical aperture 0.9) used in our study, the diameter of the incident focused laser beam and the laser power onto the sample's surface were ~1 μm and 2.3 mW, respectively. No shift due to the local heating of the sample by the laser beam was observed. Raman spectra were acquired while moving the sample stage with 0.8 μm steps in *x*- and *y*-direction, resulting in a complete mapping of the investigated areas. The exposure time was 200 ms per spectrum. By fitting these spectra with a Gauss–Lorentzian function, maps of the shifts of the first-order silicon Raman peak corresponding to internal stresses were obtained with a resolution of $\pm 0.05\ cm^{-1}$ [16,18,19]. To ensure correct interpretation of the Raman data as well as to be able to visualize small mechanical stresses, the effect of the environmental thermal variations on the silicon peak position was corrected [17]. This was done using one of the plasma lines of a Ne lamp located close to the spectrometer's entrance hole [18,23].

After the Raman measurements, the grain orientations and grain boundary types were determined by EBSD using an EDAX system attached to a TESCAN LYRA XMU scanning electron microscope (SEM). The crystal orientation is given in the $\{h\,k\,l\}<u\,v\,w>$ representation where $\{h\,k\,l\}$ is the crystal plane perpendicular to the sample normal direction (*z* axis) and $<u\,v\,w>$ is the crystal direction aligned with the transverse direction of the sample (*y*-axis) (see Figs. 2–4(b)). The inverse pole figure (unit triangle) shows the sample normal direction relative to the axes of the measured crystal. The misorientation between adjacent grains is given in the angle/axis notation, that is, the rotation angle about the axis common to both lattices to bring them into coincidence, and in terms of Σ-value, which denotes the fraction of atoms in the GB plane coincident in both lattices [24].

Finally, EBIC measurements at 20 keV beam energy were done with an EVO 40 SEM at 80 K to image most of the electrically active defects. Before the electrical characterization, the sample was chemically polished in 1 HF:2 $HNO_3$:1 $C_2H_4O_2$ solution for 5 s. The top Schottky contact consisting of a 30 nm thick Al layer was evaporated onto the sample surface, while the back ohmic contact was prepared by rubbing InGa alloy homogeneously over the back side of the sample. In order to render the inhomogeneities of recombination clearly visible, a color scale is used for the EBIC maps (see Figs. 2–4(c)). The maps represent the local EBIC signal normalized by the maximum EBIC signal.

## 3. Results

In order to illustrate the correlation between internal stresses, defect structure, and electrical activity in the EFG material, we show here three positions that contain representative examples of this correlation for the four measured samples grown under similar conditions (about 5–10 positions on each sample). These regions indicated by arrows in Fig. 1(b) are located along a typical GB that forms between two adjacent grains of {0 1 1} and {1 1 2}

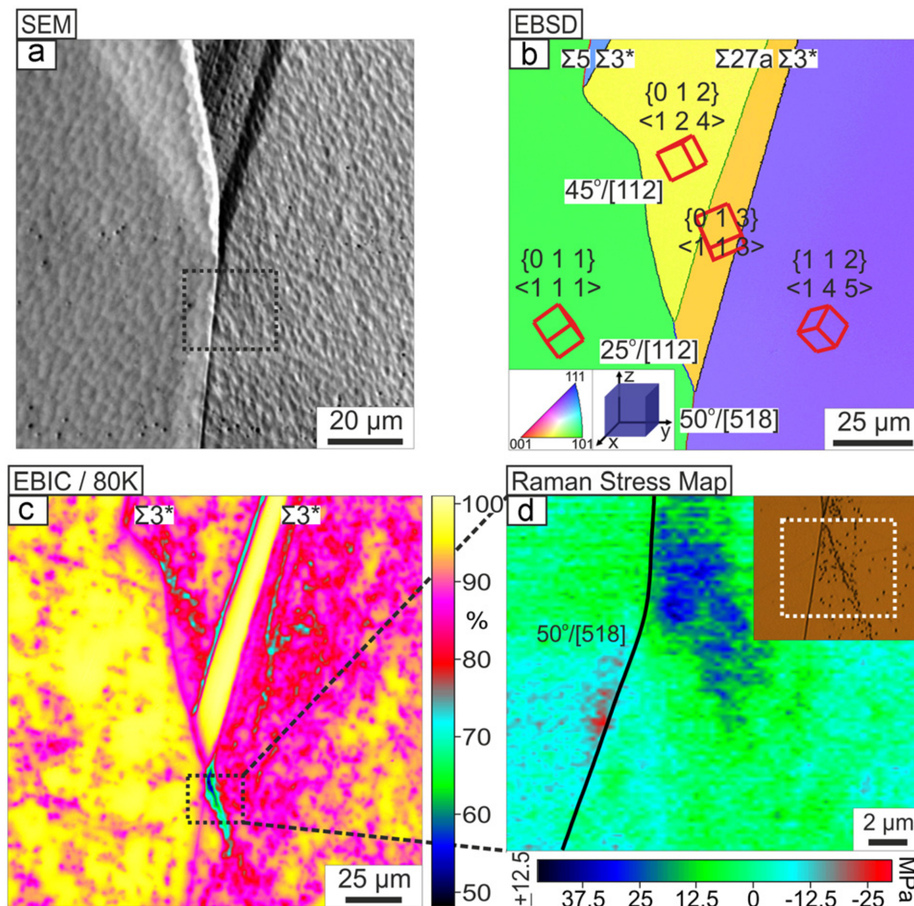


**Fig. 2.** Position (1) (a) SEM image of the as-grown EFG wafer before mechanical polishing. (b) EBSD map showing the grain orientations and GB types along with the orientation triangle and the sample reference frame. (c) EBIC image taken at 80 K where the inhomogeneous recombination activity inside grains and at GBs is mainly attributed to dislocations decorated with metallic impurities. (d) Not all dislocations visible in the defect etching image shown in the inset or measured by EBIC are accompanied by internal stresses as probed by micro-Raman. The dashed rectangle in the inset represents the Raman mapped area. At this position, the lowest EBIC current corresponds to the largest (tensile) stress.

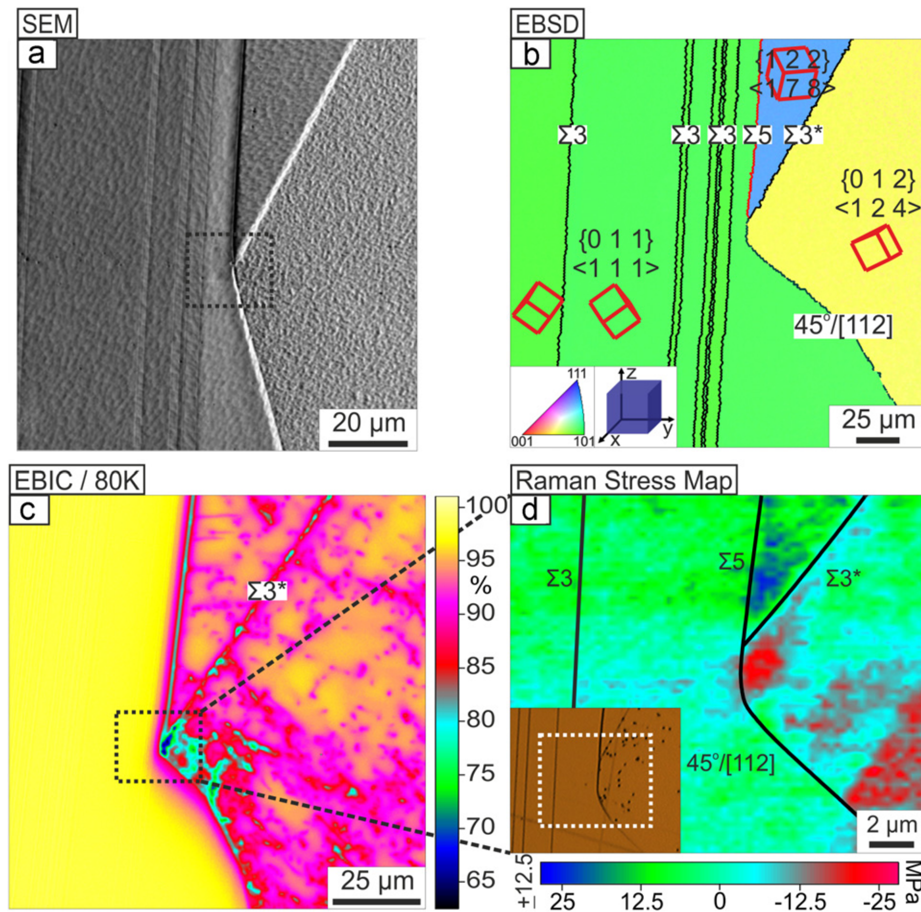


**Fig. 3.** Position (2) (a) SEM image of the as-grown EFG wafer before mechanical polishing. (b) EBSD map. (c) EBIC image where the same left hand side grain like in Fig. 2 shows at this position no electrical activity. The Σ3 GBs are either recombination-free (Σ3) or recombination-active (Σ3*), while being virtually stress-free. (d) The defect etching image in the inset indicates that the presence of dislocation etch pits on Σ3* GBs leads to electrical activity provided the dislocations are decorated with metallic impurities. Here, the highest recombination activity corresponds to the largest (compressive) stress.

orientations. They are the preferred orientations under steady-state EFG growth conditions: {0 1 1} minimizes the surface energy, while {1 1 2} occurs from the twining of {0 1 1} [25]. SEM images of the as-grown EFG wafer before mechanical polishing show no significant out-of-plane buckling at these positions, as seen in Figs. 2–4(a). Moreover, the defect configurations at these positions displayed in Figs. 2–4 including large-angle random GBs, coincidence-site lattice GBs, GB triple points, and high dislocated areas are characteristic for the typical microstructure of the EFG material.

Our defect etching experiments shown in the insets of Figs. 2–4(d) reveal, besides GBs, typical distributions of etch pits, which are formed where dislocations intersect the surface of the silicon wafer due to enhanced removal of atoms from the defective regions. The dashed rectangles in the insets as well as in Figs. 2–4(a) correspond to the Raman mapped areas. Thus, we discuss our results based on the presence of dislocations [26–28].

The EBSD, EBIC, and micro-Raman measurements at position (1) are displayed in Fig. 2. The Raman stress map shows concentrated tensile (in blue) and compressive (in red) stresses close to a large-angle random GB described by a misorientation angle/axis of 50°/[5 1 8]. Except these areas, nearly no stresses are found neither along the GB nor inside the two adjacent grains of {0 1 1}<1 1 1> and {1 1 2}<1 4 5> orientations. By comparing the stress map with the corresponding EBIC map enclosed by the rectangle in Fig. 2(c), it can be seen that not all recombination active dislocations visible at 80 K are accompanied by stresses. That is because dislocations interact with each other and tend to locally rearrange in configurations of minimum strain energy that can result in stresses or virtually no stresses [18,19,25,29]. The EBIC image in Fig. 2(c) shows an inhomogeneous electrical activity along different types of GBs as well as inside grains of different crystallographic orientations indicated in Fig. 2(b). The recombination-active Σ3 GBs {60°/[1 1 1]} in Figs. 2–4 are marked with an asterisk to distinguish them from the recombination-free Σ3 GBs in Fig. 3. All these are considered to originate from a nonuniform distribution of dislocations on GBs and inside grains, with the recombination activity strength depending on the metallic impurity decoration, intrinsic structure, type, density, and distribution of dislocations [18,21,25,30].

Fig. 3 shows the EBSD, EBIC, and micro-Raman results obtained at position (2). Like in the previous case, we did not find a one-to-one correspondence between electrically active dislocations and stresses, both exhibiting inhomogeneous spatial and magnitude distributions. Different at this position is the presence of tensile (in blue) and compressive (in red) stresses concentrated close to a GB triple point where a Σ5 GB {36.86°/[1 0 0]}, a Σ3 GB, and a large-angle random GB {45°/[1 1 2]} meet. It is worth noting that GBs of the same type, here Σ3 GBs, can be either recombination-free (Σ3) or recombination active (Σ3*), while both being nearly stress-free. Essentially, independent of the GB type, such large differences in electrical activity originate mainly from the absence or presence of recombination-active dislocations on or very close to the GB [22,26]. On the other hand, Raman measures only those configurations of dislocations (including the recombination-free dislocations) that lead to stresses. In contrast with the positions

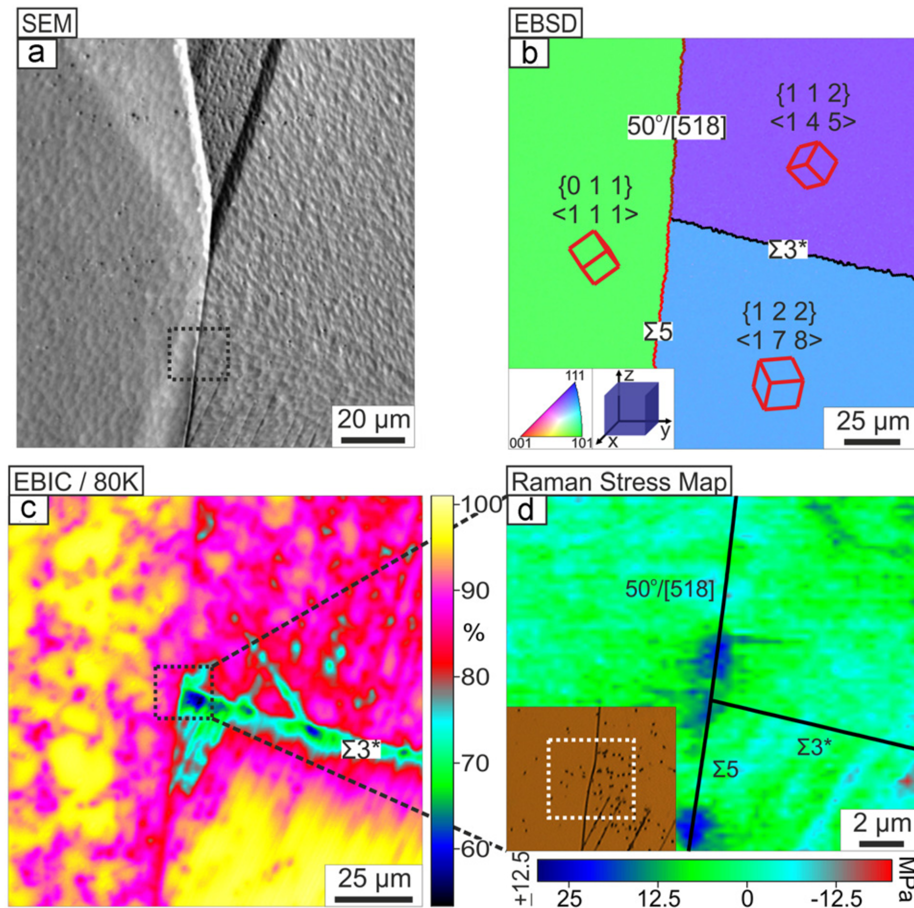


**Fig. 4.** Position (3) (a) SEM image of the as-grown EFG wafer before mechanical polishing. (b) EBSD map. (c) EBIC image where the same left hand side grain like in Figs. 2 and 3 shows recombination activity. (d) The lowest EBIC current is not accompanied by stress at this position.

(1—Fig. 2) and (3—Fig. 4), the {0 1 1} <1 1 1> left hand side grain shows no reduction in the EBIC signal at position (2). This indicates that the thermally induced stresses present during the EFG growth relaxed not through the generation of dislocations but through the formation of twins found at position (2) by EBSD [12,31].

Similar to the previous two cases, we observe nonuniform distributions of electrical activity and stresses along GBs and inside grains at position (3), as displayed in Fig. 4(c and d). However, we choose this position to show that the largest recombination activity is not always accompanied by the largest internal stresses as in the case of positions (1) and (2).

## 4. Discussions

The inhomogeneous distributions of electrical activity and internal stresses in Figs. 2–4(c and d) are discussed in detail in the following. Internal stresses are the result of the superposition between the thermally induced residual stresses, that is the thermally induced stresses at the end of crystallization and cooling processes, and the defect-related stresses. Since the EFG tubes are cut into wafers and then into small pieces as those investigated here, the thermally induced residual stresses are expected to relax to a large extent due to the creation of free surfaces [12]. Thus, in this paper, we measure mainly the internal stresses produced by defects.

Dislocations are considered to be among the most detrimental type of defects controlling not only the electrical but also the mechanical properties of silicon and other materials [18,20,26–28]. First, for the sake of simplicity, we address the spatial variation in the EBIC and micro-Raman measurements without taking into account the impurities. Dislocations are the result of plastic deformation taking place to relax thermally induced stresses. This occurs as long as plasticity is allowed by temperature and the thermal stress level is above the yield value [5,12,32]. These stresses are produced by temperature gradients, which in turn are due to nonlinear cooling and temperature dependent thermal expansion coefficients. Both are intrinsic to all silicon crystal growth methods [5,20]. In the case of EFG ribbon growth, there are two nonlinear temperature profiles: one vertical along the tube length and one horizontal along the tube width (see Fig. 1(a) and Ref. [6]).

Once dislocations are created, they can move on glide planes if the thermal activation energy (temperature above 600–700 °C in silicon) and the effective stress for dislocation motion are provided. The latter is given by the difference between the thermally induced stresses produced by the nonlinear external temperature profiles and the stresses due to short- and long-range elastic interactions between dislocations [29,33–35]. The movement of dislocations leads to further plastic deformation through their multiplication up to the point when, because of an increased dislocation density, the lattice friction overcomes the effective stress needed for moving dislocations. This state corresponds to the hardening state of the material [20,33]. Dislocations can also be removed by out-diffusion and pairwise annihilation at high temperatures [27]. In the case of EFG mc-Si material, the grain structure including the orientation, size, and geometry of the

grains as well as the kinematic constraints at GBs influence locally the nucleation, motion, multiplication, and annihilation of dislocations [3,20,34,35]. Furthermore, these mechanisms vary significantly with temperature changing continuously the density and distribution of dislocations through the change in the effective stress fields acting locally on them [33]. Consequently, in the EFG mc-Si material, there is strong local variation in intragranular and GB decorating dislocations, resulting in spatially nonuniform recombination activity and dislocation-related stresses, as shown in Figs. 2–4(c and d).

Second, we focus on the magnitude variation of the EBIC and micro-Raman measurements. In addition to the temperature and microstructure dependent interaction between dislocations in order to minimize the strain energy, their type also affects the electrical activity and residual stress states [18,21,25,33]. Typically, the so-called mixed dislocations consisting of both edge and screw segments are found in real materials [29,33]. In the isotropic elasticity theory, the elastic distortion around an edge dislocation produces both normal (compressive stresses above the slip plane and tensile below) and shear stress components, while only shear stresses occur in the case of a screw dislocation. The stress components that are zero in the isotropic approximation may become finite in elastically anisotropic materials such as silicon [18,29]. Thus, the measured micro-Raman signal is mainly the superposition of the stress fields of dislocations including all stress components. Besides the dislocation type, there are other factors that can influence the stress states such as impurity decoration, intrinsic structure, density, and distribution of dislocations [18,21,25,30]. We found stress concentrations including both tensile (in blue) up to 40 MPa and compressive (in red) up to 25 MPa ($\pm 12.5$ MPa), as displayed in Figs. 2(d) and 3(d), respectively. These local variations in the sign and values of the dislocation-related stresses in Figs. 2–4(d) are attributed to the cumulative effect of all the aforementioned factors.

These factors are also considered to be responsible for the differences in the strength of recombination activity seen in Figs. 2–4(c). We observed quite strong reduction in the EBIC signals at room temperature up to 70% (not shown), which increase with decreasing temperature. Such EBIC behavior can be explained by the interaction of shallow levels related to the strain fields of dislocations with deep levels due to metallic impurity decoration and/or intrinsic core defects at dislocations [18,28,36,37]. In this context, it is interesting to elaborate on the reasons for the EBIC signal variability at GBs of the same type as well as inside grains of similar crystallographic orientations determined by EBSD. By comparing the defect-etched optical images with the EBIC maps (see, for instance, inset of Fig. 3(d) and (c) corresponding to position (2)), we found that $\Sigma 3$ boundaries decorated by dislocation etch pits (denoted $\Sigma 3^*$) also show increased electrical activity. By contrast the $\Sigma 3$ GBs without dislocation etch pits show no recombination activity. It can be seen that despite the same GB type assignment by the EBSD software, the $\Sigma 3^*$ and $\Sigma 3$ GBs are formed between adjacent grains of different crystallographic orientations. This fact suggests distinct kinematic conditions at these $\Sigma 3$ GBs that can lead to dissimilar thermally induced stress levels resulting in the generation or absence of dislocations. Different electrical activities can be largely explained by the presence of different amounts of metallic impurities in the form of atoms or submicron precipitates in the dislocation cores or/and in the strain fields of dislocations [28,37,38]. Such decorated dislocations are also invoked to account for the very different electrical activity of the $\{0\,1\,1\} < 1\,1\,1 >$ left hand side grain, as seen in Figs. 2–4(c). Only few of them are visible in the insets of Figs. 2–4(d) because of the short etching time. The EBSD maps in Figs. 2–4(b) show that the adjacent right hand side grains exhibit similar orientations and quite similar geometries at the displayed positions. This indicates comparable kinematic constraints at these GBs. Therefore, we attribute the presence (Figs. 2(c) and 4(c)) or absence (Fig. 3(c)) of electrical activity (recombination active defects) inside the $\{0\,1\,1\} < 1\,1\,1 >$ left hand side grain to locally different thermally induced stresses resulting in different relaxation mechanisms (dislocation or twin formation) [3,6,31].

Third, we examine the correlation between internal stresses and electrical activity at the micrometer scale in the EFG material. From the Raman and EBIC maps, it is observed that the largest stresses coexist with the largest recombination at positions (1) and (2) but not at position (3). These observations can be explained as follows. It has been shown that impurity accumulation in silicon can be enhanced due to the presence of stresses [12,39]. This happens at temperatures where both impurities and dislocations are mobile, while the driving force is the superposition of thermal stresses and the stress fields of dislocations. The degree of thermal stress relaxation by dislocation formation varies locally affecting the dislocation density and the amount of thermally induced residual stress. The final result can be an increased electrical activity at regions of higher dislocation densities and stresses (thermal or/and from dislocations), as at positions (1) and (2). Here, dislocations are spatially distributed in such a way that their stress fields cancel partially or not at all so that an overall long-range stress field from these dislocations is measured by micro-Raman. The dislocations arranged in configurations in which their stress fields cancel totally (or below the detection limit of our Raman spectrometer of $\pm 12.5$ MPa) are only visible by EBIC (when recombination-active) but not by micro-Raman, as at position (3). Our results indicate that internal stresses of several tens of MPa do not influence the minority carrier recombination in EFG mc-Si, which is consistent with reports on block-cast mc-Si [18,32]. Indeed, comparably high stresses of up to 1.2 GPa are necessary in silicon in order to enhance the carrier mobility in the transistor channel through the band structure modification and the effective mass reduction [40].

The results presented above along with those obtained from all not show measured samples and positions are displayed in Fig. 5 in the form of point-by-point correlation and double histogram analysis of the micro-Raman and EBIC measurements. It is found

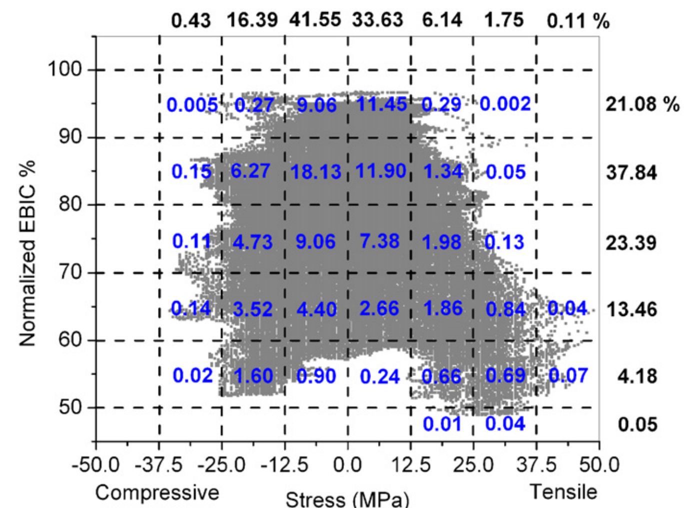


**Fig. 5.** Point-by-point correlation of internal stress and electrical activity from all micro-Raman and EBIC measurements. The lower the EBIC signal, the higher the recombination activity. The numbers inside the figure represent the percent of the data points for particular combinations of stress and EBIC values based on double histogram analysis. The sums of the percentages for the same EBIC and stress value bins are shown on right and top of the figure, respectively.

statistically based on the data in Fig. 5 that the sample/position to sample/position variations in internal stresses and recombination activity on the micrometer scale are mainly caused by the locally different defect structure and defect impurity decoration in agreement with photoelasticity and photoluminescence measurements on the macro-scale (wafer level) [2,8,10,12]. These structural variations on the micrometer scale result in efficiency variations on the macro-scale of $\pm 0.2\%$ after solar cell in-line processing of wafers cut from the same 6.5 m long EFG octagonal tube. The difference in electrical activity ($y$-axis) for a fixed internal stress level ($x$-axis) indicates dissimilar impurity accumulation due to locally different internal stresses at temperatures allowing the stress-induced motion of impurities.

Although we focus here only on the EFG mc-Si ribbons, the combined application of the complementary analytical methods used in this paper (micro-Raman, EBIC, defect etching, and EBSD) can be extended to other types of silicon wafers cut from, e.g., directionally solidified ingots or string ribbons. The current observations about the correlation between internal stresses, recombination activity, and microstructure are similar to our previous reports on block-cast mc-Si wafers [15,18] and consistent with other works involving various mc-Si materials and experimental approaches [2,8,12,32]. Recently, we demonstrated the combined application of micro-Raman and photoelasticity methods for characterizing internal stresses and their relation to defects at different length scales in block-cast mc-Si [15]. This approach will also be applied to the EFG ribbon material to study separately the concentrated stress fields of defects and the extended thermally induced residual stresses in relation to the electrical activity.

Finally, we discuss the practical impact of our study on increasing the mechanical stability and conversion efficiency of solar cells. We have found that the interaction between dislocations can lead to the reduction in internal stresses. This finding has two important implications. From the mechanical yield point of view, the lower the internal stress levels, the lower the fracture rates during manufacturing and manipulation of wafers, solar cells, and modules. From the perspective of electrical performance, low stressed or stress-free defect configurations are less likely to promote the gathering of metallic impurities at single dislocations as well as to generate new recombination active dislocations under external mechanical and thermal stresses. Therefore, it is worth exploring temperature profiles that facilitate the interaction between structural defects during the crystallization process and/or during the high temperature solar cell processing steps. This applies not only to the EFG ribbon growth but also to other crystal growth procedures, e.g. directional solidification or string ribbon. The understanding and control of the interplay between stresses and defects and their effect on impurities represent also a topic of fundamental research having potential for increasing the electrical performance of solar cells [41].

## 5. Conclusions

The interplay between internal stresses originating from dislocations, recombination activity, and microstructure has been studied at identical positions in as-grown EFG mc-Si ribbon material by combining micro-Raman, EBIC, defect etching, and EBSD techniques. The distributions of internal stresses and electrical activity are found to vary both spatially and in magnitude. They are inhomogeneous along the same GB, along different GBs of similar character as well as inside the same grain and inside different grains of similar orientations. These variations are attributed to the presence of dislocations, namely to the cumulative effect of their impurity decoration, intrinsic structure, type, density, and spatial arrangement on GBs and inside grains. Internal tensile or compressive stresses of several tens of MPa are considered not to affect the electrical activity by band structure modification but they can enhance the accumulation of metallic impurities and consequently the minority carrier recombination. By tuning the crystallization process, wafer manufactures can use the interaction between dislocations driven by the strain energy minimization to produce mechanically stronger wafers and cells and to prevent impurity precipitation at dislocations that should lead to improved energy conversion efficiencies.

## Acknowledgments

This work was financially supported by the German Federal Ministry for the Environment, Nature Conservation, and Nuclear Safety and all the industry partners within the research cluster SolarFocus (0327650A+D) and by the Max-Planck Society within the project Nanostress. The content of this publication is the responsibility of the authors.

## References

[1] G. Hahn, A. Schönecker, New crystalline silicon ribbon materials for photovoltaics, J. Phys.: Condens. Matter 16 (2004) R1615–R1648.
[2] B. Mackintosh, A. Seidl, M. Ouellette, B. Bathey, D. Yates, J. Kalejs, Large silicon crystal hollow-tube growth by the edge-defined film-fed growth (EFG) method, J. Cryst. Growth 287 (2006) 428–432.
[3] M. Müller, B. Birkmann, F. Mosel, I. Westram, A. Seidl, Silicon EFG process development by multiscale modeling, J. Cryst. Growth 312 (2010) 1397–1401.
[4] H.J. Scheel, P. Capper, Crystal Growth Technology: From Fundamentals and Simulation to Large-Scale Production, Wiley-VCH, 2008 (Chapters 5 and 10).
[5] H. Behnken, D. Franke, H. Kasjanow, A. Nikanorov, A. Seidl, 3D-simulation of EFG process and deformation of the growing silicon tube, in: Proceedings of the 4th IEEE World Conference on Photovoltaic Energy Conversion, 2006, pp. 1175–1178.
[6] B. Birkmann, S. Günther, F. Mosel, M. Müller, I. Westram, A. Seidl, Growth of 200 micron thin EFG dodecagonal tubes: benefit of numerical simulation for process optimization, in: Proceedings of the 23rd European Photovoltaic Solar Energy Conference, 2008, pp. 1080–1083.
[7] P.J. Withers, Residual stress and its role in failure, Rep. Prog. Phys. 70 (2007) 2211–2264.
[8] S. He, S. Danyluk, I. Tarasov, S. Ostapenko, Residual stresses in polycrystalline silicon sheet and their relation to electron-hole lifetime, Appl. Phys. Lett. 89 (2006) 111909.
[9] X.F. Brun, S.N. Melkote, Analysis of stresses and breakage of crystalline silicon wafers during handling and transport, Sol. Energy Mater. Sol. Cells 93 (2009) 1238–1247.
[10] M.C. Brito, J.M. Alves, J.M. Serra, R.M. Gamboa, C. Pinto, A.M. Vallera, Measurement of residual stress in EFG ribbons using a phase-shifting IR photoelastic method, Sol. Energy Mater. Sol. Cells 87 (2005) 311–316.
[11] H.J. Möller, C. Funke, A. Lawerenz, S. Riedel, M. Werner, Oxygen and lattice distortions in multicrystalline silicon, Sol. Energy Mater. Sol. Cells 72 (2002) 403–416.
[12] V. Ganapati, S. Schoenfelder, S. Castellanos, S. Oener, R. Koepge, A. Sampson, M.A. Marcus, B. Lai, H. Morhenn, G. Hahn, J. Bagdahn, T. Buonassisi, Infrared birefringence imaging of residual stress and bulk defects in multicrystalline silicon, J. Appl. Phys. 108 (2010) 063528.
[13] T. Buonassisi, S. Reitsma, R. Sweeney, M.D. Pickett, W. Huang, J. Lesniak, M.L. Spencer, Evolution of stresses in wafer bulks and edges during industrial solar cell processing, in: Proceedings of the 22nd European Photovoltaic Solar Energy Conference, 2007, pp. 813–815.
[14] G. Sarau, S. Christiansen, R. Lewandowska, B. Roussel, Future of Raman in PV development, in: Proceedings of the 35th IEEE PVSC, 2010, pp. 001770–001775.
[15] G. Sarau, A. Bochmann, S. Christiansen, S. Schönfelder, Stresses and their relation to defects in multicrystalline solar silicon, in: Proceedings of the 35th IEEE PVSC, 2010, pp. 000699–000703.
[16] M. Becker, H. Scheel, S. Christiansen, H.P. Strunk, Grain orientation, texture, and internal stress optically evaluated by micro-Raman spectroscopy, J. Appl. Phys. 101 (2007) 063531.
[17] I. De Wolf, Micro-Raman spectroscopy to study local mechanical stress in silicon integrated circuits, Semicond. Sci. Technol. 11 (1996) 139–154.
[18] G. Sarau, M. Becker, S. Christiansen, M. Holla, W. Seifert, Micro-Raman mapping of residual stresses at grain boundaries in multicrystalline block-cast silicon solar cell material: their relation to the grain boundary

microstructure and recombination activity, in: Proceedings of the 24th European Photovoltaic Solar Energy Conference, 2009, pp. 969–973.
[19] G. Sarau, M. Becker, A. Bochmann, A. Gawlik, G. Andrä, S. Christiansen, Evolution of residual stress and its relation to microstructure in multicrystalline silicon thin film solar cells on glass prepared by combined laser crystallization and solid phase epitaxy, in: Proceedings of the 24th European Photovoltaic Solar Energy Conference, 2009, pp. 2494–2499.
[20] H. Behnken, Simulation of the development of dislocation density in multicrystalline silicon during crystallization processes, in: Proceedings of the 24th European Photovoltaic Solar Energy Conference, 2009, pp. 1281–1285.
[21] C.T. Ho, D.B. Sandstrom, C.E. Dubé, Classification of macroscopic defects contained in p-type EFG ribbon silicon, Solid-State Electron. 29 (1986) 495–503.
[22] F. Secco, D′. Aragona, Dislocation etch for (1 0 0) planes in silicon, J. Electrochem. Soc. 119 (1972) 948–951.
[23] G. Sarau, M. Becker, A. Berger, J. Schneider, S. Christiansen, Stress distribution in polycrystalline silicon thin film solar cells on glass measured by micro-Raman spectroscopy, Mater. Res. Soc. Symp. Proc. 1024E (2007) 1024–A07-04.
[24] H. Grimmer, W. Bollmann, D.H. Warrington, Coincidence-site lattices and complete pattern-shift in cubic crystals, Acta Crystallogr. A30 (1974) 197–207.
[25] K. Yang, G.H. Schwuttke, T.F. Ciszek, Structural and electrical characterization of crystallographic defects in silicon ribbons, J. Cryst. Growth 50 (1980) 301–310.
[26] H.Y. Wang, N. Usami, K. Fujiwara, K. Kutsukake, K. Nakajima, Microstructures of Si multicrystals and their impact on minority carrier diffusion length, Acta Mater. 57 (2009) 3268–3276.
[27] K. Hartman, M. Bertoni, J. Serdy, T. Buonassisi, Dislocation density reduction in multicrystalline silicon solar cell material by high temperature annealing, Appl. Phys. Lett. 93 (2008) 122108.
[28] T. Buonassisi, A.A. Istratov, M.D. Pickett, M.A. Marcus, T.F. Ciszek, E.R. Weber, Metal precipitation at grain boundaries in silicon: dependence on grain boundary character and dislocation decoration, Appl. Phys. Lett. 89 (2006) 042102.
[29] D. Hull, D.J. Bacon, Introduction to Dislocations, Butterworth-Heinemann, 2001 (Chapters 4 and 9).
[30] J. Chen, T. Sekiguchi, D. Yang, F. Yin, K. Kido, S. Tsurekawa, Electron-beam-induced current study of grain boundaries in multicrystalline silicon, J. Appl. Phys. 96 (2004) 5490.
[31] Y. Han, L. Lin, New insight into the origin of twin and grain boundary in InP, Solid State Commun. 110 (1999) 403–406.
[32] J. Chen, B. Chen, T. Sekiguchi, M. Fukuzawa, M. Yamada, Correlation between residual strain and electrically active grain boundaries in multicrystalline silicon, Appl. Phys. Lett. 93 (2008) 112105.
[33] J. Cochard, I. Yonenaga, S. Gouttebroze, M. M'Hamdi, Z.L. Zhang, Constitutive modeling of intrinsic silicon monocrystals in easy glide, J. Appl. Phys. 107 (2010) 033512.
[34] J. Cochard, S. Gouttebroze, S. Dumoulin, M. M'Hamdi, Z.L. Zhang, A multicrystal model for the viscoplastic deformation of Silicon at high temperature, in: Proceedings of the 23rd European Photovoltaic Solar Energy Conference, 2008, pp. 1919–1923.
[35] J. Cochard, S. Gouttebroze, S. Dumoulin, M. M'Hamdi, Z.L. Zhang, Mechanical modelling of impure silicon materials, in: Proceedings of the 24th European Photovoltaic Solar Energy Conference, 2009, pp. 1240–1243.
[36] V. Kveder, M. Kittler, W. Schröter, Recombination activity of contaminated dislocations in silicon: a model describing electron-beam-induced current contrast behaviour, Phys. Rev. B 63 (2001) 115208.
[37] T. Buonassisi, A.A. Istratov, M.D. Pickett, M. Heuer, J.P. Kalejs, G. Hahn, M.A. Marcus, B. Lai, Z. Cai, S.M. Heald, T.F. Ciszek, R.F. Clark, D.W. Cunningham, A.M. Gabor, R. Jonczyk, S. Narayanan, E. Sauar, E.R. Weber, Chemical natures and distributions of metal impurities in multicrystalline silicon materials, Prog. Photovolt.: Res. Appl. 14 (2006) 513–531.
[38] M. Seibt, R. Khalil, V. Kveder, W. Schröter, Electronic states at dislocations and metal silicide precipitates in crystalline silicon and their role in solar cell materials, Appl. Phys. A 96 (2009) 235–253.
[39] C. Ahn, N. Bennett, S.T. Dunham, N.E.B. Cowern, Stress effects on impurity solubility in crystalline materials: a general model and density-functional calculations for dopants in silicon, Phys. Rev. B 79 (2009) 073201.
[40] J. Chung, G. Lian, L. Rabenberg, Local strain measurement in a strain-engineered complementary metal-oxide-semiconductor device by geometrical phase analysis in the transmission electron microscope, Appl. Phys. Lett 93 (2008) 081909.
[41] M.I. Bertoni, D.M. Powell, M.L. Vogl, S. Castellanos, A. Fecych, T. Buonassisi, Stress-enhanced dislocation density reduction in multicrystalline silicon, Phys. Status Solidi RRL 5 (2011) 28–30.